scientific reports

OPEN

Core and surface structure and magnetic properties of mechano-synthesized LaFeO$_3$ nanoparticles and their Eu^{3+}-doped and Eu^{3+}/Cr^{3+}-co-doped variants

R. T. Al-Mamari[1], H. M. Widatallah[1✉], M. E. Elzain[1], A. M. Gismelseed[1], A. D. Al-Rawas[1], S. H. Al-Harthi[1], M. T. Z. Myint[1], N. Al-Saqri[1] & M. Al-Abri[2]

The core and surface structure and magnetic properties of mechano synthesized LaFeO$_3$ nanoparticles (30–40 nm), their Eu^{3+}-doped (La$_{0.70}$Eu$_{0.30}$FeO$_3$), and Eu^{3+}/Cr^{3+} co-doped (La$_{0.70}$Eu$_{0.30}$Fe$_{0.95}$Cr$_{0.05}$O$_3$) variants are reported. Doping results in a transition from the *O'-type* to the *O-type* distorted structure. Traces of reactants, intermediate phases, and a small amount of Eu^{2+} ions were detected on the surfaces of the nanoparticles. The nanoparticles consist of antiferromagnetic cores flanked by ferromagnetic shells. The Eu^{3+} dopant ions enhance the magnetization values relative to those of the pristine nanoparticles and result in magnetic susceptibilities compatible with the presence of Eu^{3+} van Vleck paramagnetism of spin–orbit coupling constant (λ = 363 cm^{-1}) and a low temperature Curie–Weiss like behavior associated with the minority Eu^{2+} ions. Anomalous temperature-dependent magnetic hardening due to competing magnetic anisotropy and magnetoelectric coupling effects together with a temperature-dependent dopant-sensitive exchange bias, caused by thermally activated spin reversals at the core of the nanoparticles, were observed.

The orthorhombically distorted perovskite-related rare-earth orthoferrite materials of the composition (RE)FeO$_3$, where RE is a rare earth ion, are technologically attractive due to their physicochemical properties that render them of potential usage in a host of applications[1–7]. One such a material is lanthanum orthoferrite, LaFeO$_3$, that crystallizes in the space group *Pbnm* (# 62) with lattice constants a = 5.556 Å, b = 5.565 Å and c = 7.862 Å[5]. The La^{3+} and Fe^{3+} ions, respectively, occupy the so-called A sites and the six O^{2-} coordinated octahedral B sites (BO$_6$). Unlike cubic perovskites, where the A sites are 12 O^{2-}-coordinated cuboctahedra (AO$_{12}$), the orthorhombically distorted (RE)FeO$_3$ (RE = from Pr to Lu) compounds possess 8 O^{2-}-coordinated A sites (AO$_8$). However, in *bulk* LaFeO$_3$, Marezio et al.[8] have shown that the difference between the distances of the La^{3+} ion to its eighth and ninth nearest O^{2-} neighbors, namely, 2.805 Å and 3.041 Å, respectively, is insignificant. Hence, the A sites in LaFeO$_3$ are considered AO$_9$ polyhedra. The magnetic ordering of the high-spin Fe^{3+} cations in LaFeO$_3$ results in G-*type* antiferromagnetism (AFM) which is accompanied by a weak canted ferromagnetic (FM) component. The high Néel temperature (T$_N$) of ~ 740 K reported for the material is a consequence of the strong Fe^{3+}–O^{2-}–Fe^{3+} super-exchange coupling[1,9]. The other inherent properties of LaFeO$_3$, which are important from an applied viewpoint, include thermal, electrical, magneto-optical, and high chemical stability, in addition to multiferroicity[2,4,5,10].

To extend the technological utilization of LaFeO$_3$, some researchers have attempted to modify its properties by producing it either in the form of nanoparticles or by introducing substituents for La^{3+} and/or Fe^{3+} cations[2–4]. In this respect, novel magnetic properties, such as magnetic exchange bias (*EB*), superparamagnetism, and spin glass behavior, have been reported for LaFeO$_3$ nanoparticles of sizes in the 10–60 nm range[2,3,9–11]. Such proper-ties, which are of interest for various applications, including magnetic sensors, spintronics, and data storage

[1]Physics Department, Sultan Qaboos University, Al-Khoudh, P.O. Box 36, Muscat 123, Oman. [2]Nanotechnology Research Center, Sultan Qaboos University, Al-Khoudh, P.O. Box 17, Muscat 123, Oman. ✉email: hishammw@squ.edu.om

devices[1,4,6], could be further tuned by single-site cation doping. In connection with this, we note that when soft chemistry methods were used to introduce Na^+, Zn^{2+}, Sb^{3+} or Ce^{4+} as sole substituents for La^{3+} in $LaFeO_3$ nanoparticles, the coercivity (H_c) was found to depend on the dopant concentration[3,5,11]. Doping with single cations such as Na^+ and Zn^{2+} has affected the superparamagnetic behavior of the nanoparticles, as both the blocking and relaxation temperatures were found to decrease[3,9]. Of interest to us in this paper is the work of Hosseini et al. who reported the use of the sol–gel route to form Eu^{3+}-doped $LaFeO_3$ nanoparticles of the composition $La_{1-x}Eu_xFeO_3$ ($x \leq 0.15$) without elaborating on how Eu^{3+}-doping affects their structural and magnetic properties[12]. Similarly, the substitution of Fe^{3+} in $LaFeO_3$ nanoparticles with transition metal (TM) cations has been an active area of research[4,6,10]. For instance, a spin-glass-like freezing temperature and cluster-spin behavior were reported when Mn^{3+} and Cr^{3+} were used as substituents for Fe^{3+} in $LaFeO_3$ nanoparticles[13,14]. *EB* behavior has been reported to be barely noticeable when substituting La^{3+} cations with Zn^{2+} in $LaFeO_3$ nanoparticles[3,10]. Ferromagnetically weak single-domain $LaFeO_3$ nanoparticles with particle size-dependent H_c were reported when Fe^{3+} ions were partially substituted[4] by Ti^{4+}. Recently, we have shown that Ru^{3+}-doping modifies the properties of mechano-synthesized $LaFe_{1-x}Ru_xO_3$ nanoparticles, resulting in Jahn–Teller-like distortion, a size-dependent hyperfine magnetic field, and a monotonic decrease in the optical band gap with increasing Ru^{3+} content[6]. In addition, the structure of the mechano-synthesized $LaFe_{1-x}Ru_xO_3$ nanoparticles was found to index to the *O′-type* perovskite structure with the lattice parameters related according to $c/\sqrt{2} < a < b$ as opposed to the *O-type* perovskite structure of bulk $LaFeO_3$ wherein $a < c/\sqrt{2} < b$[6]. These modifications are associated with the route of mechano-synthesis, which is known to form nanoparticles with a non-uniform core–shell structure in which the exchange interactions between the inner crystalline core and an outer disordered or amorphous shell often result in novel physical properties[15,16]. To the best of our knowledge, few studies have been devoted to the case in which both La^{3+} and Fe^{3+} cations in $LaFeO_3$ nanoparticles are concurrently substituted[17–19]. Such co-doping was found to lead to notable changes in the magnetic and ferroelectric properties, as was shown for the $La_{0.8}Sr_{0.2}Fe_{1-x}Cu_xO_3$, $La_{0.9}Dy_{0.1}Fe_{0.9}Ti_{0.1}O_3$ and $La_{1-x}Dy_xFe_{1-y}Mn_yO_3$ nanoparticles. In a previous study on mechano-synthesized nanoparticles of the isostructural compound $EuFeO_3$, co-doped with Nd^{3+} and Cr^{3+} with the composition $Nd_{0.33}Eu_{0.67}Fe_{1-x}Cr_xO_3$, we reported an unusual crystal distortion wherein Eu^{3+} and Fe^{3+} cations exchange their normal expected A and B sites and novel magnetic properties[15].

In this paper, we report on the synthesis of $LaFeO_3$, $La_{0.7}Eu_{0.3}FeO_3$ and $La_{0.7}Eu_{0.3}Fe_{0.95}Cr_{0.05}O_3$ nanoparticles using a mechanical milling route. We then systematically study the effect of Eu^{3+}-doping and Eu^{3+}/Cr^{3+} co-doping on the structural and magnetic properties of the synthesized nanoparticles. Of special interest to us is studying the contribution of the majority Eu^{3+} and minority Eu^{2+} ions detected on the intrinsic magnetic properties of the nanoparticles. As the investigated compounds have AFM ground states, it is important to carefully synthesize them as single phases so as to eliminate any contribution of Fe or Fe-oxide impurities on these magnetic properties. The experimental techniques used include X-ray diffraction (XRD), Fourier transform infrared spectroscopy (FT-IR) and ^{57}Fe Mössbauer spectroscopy, X-ray photoelectron spectroscopy (XPS) and vibrating sample (VSM) magnetometery.

Materials and methods

$LaFeO_3$, $La_{0.70}Eu_{0.30}FeO_3$ and $La_{0.70}Eu_{0.30}Fe_{0.95}Cr_{0.05}O_3$ nanoparticles were prepared starting from stoichiometric mixtures of high-purity α-Fe_2O_3, La_2O_3, Eu_2O_3 and Cr_2O_3 that were subjected to mechanical milling for different times using a Fritch D-55743 P6 milling machine with tungsten carbide vial (250 mL) and balls. The milling speed was 300 rpm, and the ball-to-powder mass ratio was 15: 1. A Carbollite (HTF 1800) furnace was used to heat the pre-milled mixtures for 10 h at various temperatures to achieve single-phased final products. XRD measurements were performed using an X'Pert PRO PANanalytical diffractometer where the Cu-K_α radiation ($\lambda = 1.5406$ Å) was employed in the 2θ-range of 20.00–80.00° at the rate of 0.02° per second. The GSAS program was used to perform XRD Rietveld refinements[20]. A JEM-1400-JEOL system, operating at 200 kV, was used to obtain high-resolution transmission electron microscopy (HRTEM) images. A PerkinElmer SpectraOne system was used to collect FT-IR spectra in the range 500–4000 cm^{-1} with a signal resolution of 4 cm^{-1} for 40 scans. ^{57}Fe Mössbauer measurements were done at 298 K and 78 K with a conventional constant acceleration spectrometer using the 14.4 keV gamma ray provided by a 50 mCi ^{57}Co/Rh source operating in transmission mode. The isomer shift values are quoted relative to α-Fe at 298 K. An Omicron NanoTechnology MXPS system (Scienta Omicron, Germany) employing the Al Kα radiation ($hv = 1486.6$ eV) was used to collect XPS spectra. The C 1s reference peak, at the binding energy of 284.6 eV, was used for binding energy calibration, and the data was fitted with the CasaXPS[21]. The VSM magnetometer option of a Quantum Design PPMS system was used to record the thermal dependence of magnetization. The measurements were carried out in both the field cooling (FC) and zero field cooling (ZFC) modes under an external magnetic field of 50 kOe in the 4–300 K temperature range. ZFC magnetic hysteresis loops were obtained at different temperatures and applied fields of up to 9 T.

Results and discussion
Mechano-synthesis and crystal structure

The XRD patterns shown in Fig. 1 indicate that the formation of single-phase $LaFeO_3$ and that of its Eu^{3+}-doped $LaFeO_3$ and Eu^{3+}/Cr^{3+} co-doped $LaFeO_3$ ($La_{0.70}Eu_{0.30}Fe_{0.95}Cr_{0.05}O_3$) variants are attained after heating the corresponding 80 h pre-milled reactants' mixtures at 600 °C (10 h) and 700 °C (10 h), respectively. These temperatures are *ca.* 600–700 °C lower than the ones reported for the formation of $LaFeO_3$ and its cation-doped modifications using the conventional solid-state routes[22]. It is obvious from the TEM images shown in Fig. 2 that the three materials are composed of semi-spherical nanoparticles that tend to agglomerate. The $LaFeO_3$ sample exhibits the widest particle size distribution with the mean particle size of (40 ± 10) nm relative to both $La_{0.70}Eu_{0.30}FeO_3$ and $La_{0.70}Eu_{0.30}Fe_{0.95}Cr_{0.05}O_3$ (30 ± 10) nm. The results of the XRD Rietveld refinements, where in the case of the

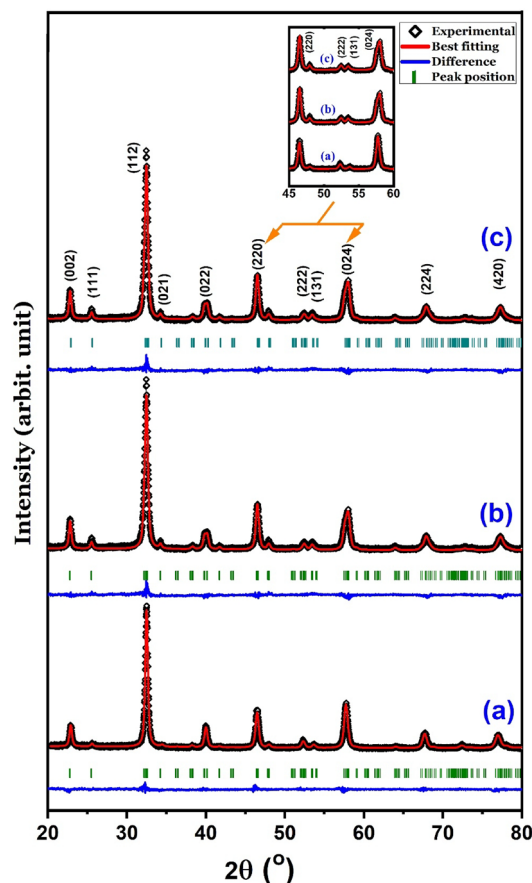**Figure 1.** Observed, calculated and difference of the XRD patterns for the (**a**) $LaFeO_3$, (**b**) $La_{0.70}Eu_{0.30}FeO_3$, and (**c**) $La_{0.70}Eu_{0.30}Fe_{0.95}Cr_{0.05}O_3$ samples. The Miller indices of each peak are given in the form of (*hkl*) and the blue bars indicate the positions of Bragg's reflection peaks. The inset shows the relative intensity reversal of the (220) and (024) peaks.
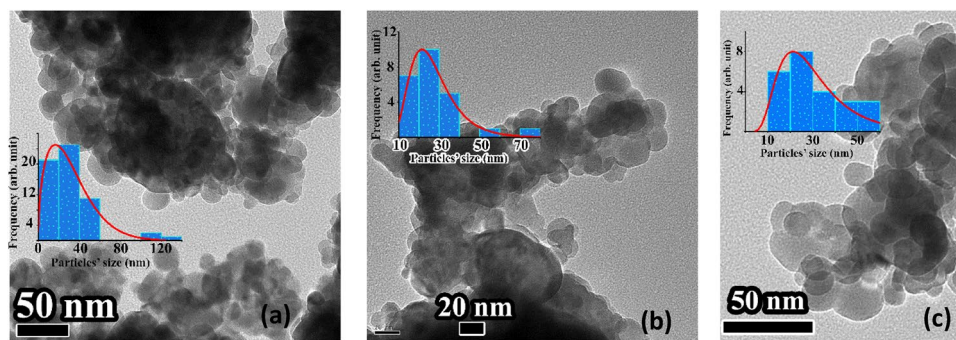

Figure 2. TEM images of the (**a**) $LaFeO_3$, (**b**) $La_{0.70}Eu_{0.30}FeO_3$, and (**c**) $La_{0.70}Eu_{0.30}Fe_{0.95}Cr_{0.05}O_3$ nanoparticles. The insets are the histograms of the particle size distribution. The solid line is the fit to the log-normal size distribution.

doped samples a common position for the La^{3+} and Eu^{3+} ions was assumed and a temperature factor to account for their disorder was included, are also shown in Fig. 1, Tables 1 and 2. It follows that each nanomaterial is structurally indexable to an orthorhombic perovskite-related phase (space group *Pbnm*)[5,7]. As the microstrain values for the doped $LaFeO_3$ samples (Table 2) are too small to be considered a factor contributing to the structural distortion associated with apparent broadened peaks relative the ones expected for the corresponding bulk samples, we attribute the broadening to lattice dislocations and surface disorder associated with crystallite size reduction to the nanometer scales[23]. The relatively large values of the microstrain in the $La_{0.70}Eu_{0.30}FeO_3$ and

Parameter	$LaFeO_3$	$La_{0.70}Eu_{0.30}FeO_3$	$La_{0.70}Eu_{0.30}Fe_{0.95}Cr_{0.05}O_3$
a (Å)	5.5549(2)	5.5019(5)	5.5006(2)
b (Å)	5.5608(1)	5.5682(2)	5.5671(4)
c (Å)	7.8472(3)	7.8089(6)	7.8067(1)
c/2 (Å)	5.5488(2)	5.5217(5)	5.5202(3)
Volume (Å)^3	242.396(1)	239.234(3)	239.056(4)
Calc. density (g/cm^3)	6.652(4)	6.849(1)	6.848(5)
Crystallite size (nm)	31(1)	28(1)	36(1)
Microstrain (%)	0.000(2)	0.20(2)	0.58(3)
(Fe/Cr)-O1 (Å)	2.002(9)	1.9818(2)	1.9705(2)
(Fe/Cr)-O2 (Å)	1.990(3)	1.9120(2)	1.9243(2)
(Fe/Cr)-O2 (Å)	2.005(3)	2.1060(2)	2.1209(2)
(Fe/Cr)-O1-(Fe/Cr) (°)	156.931(1)	160.182(2)	164.130(2)
(Fe/Cr)-O2-(Fe/Cr) (°)	161.621(1)	153.827(2)	150.595(3)
O1-(Fe/Cr)-O2 (°)	89.4, 87.7	85.3, 89.4	79.4, 84.9
O2-(Fe/Cr)-O2 (°)	89.2, 90.8	88.2, 91.8	87.1, 92.9
(Fe/Cr)O$_6$ volume (Å)^3	10.569 (2)	10.599(4)	10.493(3)

Table 1. The structural parameters extracted from the Rietveld refinement of XRD data for the $LaFeO_3$, $La_{0.70}Eu_{0.30}FeO_3$ and $La_{0.70}Eu_{0.30}Fe_{0.95}Cr_{0.05}O_3$ nanoparticles recorded at room temperature. Space group: *Pbnm* (62) and the R-Factors have their normal significance and relate to regions of the profile at which Bragg peaks contribute. $R_p < 7.91\%$, $R_{wp} < 7.99\%$, $R_{exp} < 6.77\%$, $\chi^2 \sim 1.483$. (Fe/Cr)-O is bond length; (Fe/Cr)-O-(Fe/Cr) and O-(Fe/Cr)-O are angles. The O2 oxygen ions are equatorial to Fe^{3+}, while the O1 oxygen ions are axial.

Ion and site/structural parameter	$LaFeO_3$	$La_{0.70}Eu_{0.30}FeO_3$	$La_{0.70}Eu_{0.30}Fe_{0.95}Cr_{0.05}O_3$
La^{3+} in 4c(x y ¼)			
x/a	− 0.0029(1)	− 0.0098(1)	− 0.0093(2)
y/b	0.0250(4)	0.0359(4)	0.0366(2)
Eu^{3+} in 4c(x y ¼)			
x/a	–	− 0.0098(1)	− 0.0093(2)
y/b	–	0.0359(4)	0.0366(2)
Occupancy of La^{3+}:Eu^{3+}	1.00:0.00		
Fe^{3+}/Cr^{3+} in 4b(0 ½ 0)			
Occupancy of Fe^{3+}:Cr^{3+}	1.00:0.00		
$O^{2−}$ (1) in 4c(x y ¼)			
x/a	0.0591(1)	0.0574(1)	0.0411(1)
y/b	0.4764(4)	0.4768(3)	0.4763(5)
$O^{2−}$(2) in 8d(x y z)			
x/a	− 0.2731(3)	− 0.2772(1)	− 0.2665(3)
y/b	0.2852(1)	0.3017(6)	0.2960(4)
z/c	0.0364(4)	0.0426(5)	0.0590(5)

Table 2. The fractional coordinates of the ions in the $LaFeO_3$, $La_{0.70}Eu_{0.30}FeO_3$ and $La_{0.70}Eu_{0.30}Fe_{0.95}Cr_{0.05}O_3$ nanoparticles extracted from the Rietveld refinement of the XRD data obtained at room temperature.

$La_{0.70}Eu_{0.30}Fe_{0.95}Cr_{0.05}O_3$ samples, relative to that of the $LaFeO_3$ sample, are obviously induced by cationic doping and co-doping. The data given in Tables 1 and 2 were used in combination with VESTA software[24] to draw the polyhedra of the crystal structure of $LaFeO_3$ with the ionic positions, bond lengths, and angles shown in Fig. 3.

For the $LaFeO_3$ nanoparticles, the difference between the distances of La^{3+} to its eighth and ninth nearest $O^{2−}$ neighbors, 2.527 Å and 3.028 Å, is larger than that expected for bulk $LaFeO_3$ mentioned earlier[8,10]. This, in turn, justifies the conclusion that the La^{3+} polyhedron at the A-site of the $LaFeO_3$ nanoparticles is LaO_8 rather than LaO_{12} as expected for *bulk* $LaFeO_3$[8,10]. This result indicates that the change in the La^{3+} coordination number is strongly instigated by the weakening of ionic exchange interactions at the surface of the nanoparticles. From Table 1, it can be seen that the Fe–O1 bond lengths vary coincidentally with the FeO_6-volumes. There was no cationic site exchange similar to that we previously reported for $EuFe_xCr_{1−x}O_3$ nanocrystalline particles using a similar mechano-synthesis regime[25]. The fact that the lattice constants of the $LaFeO_3$ nanoparticles are slightly smaller than those of their bulk counterparts cited above[22] may be attributed to the dislocations and disorder induced on the surface layers of the nanoparticles. The FeO_6 octahedra in the $LaFeO_3$ nanoparticles (Fig. 3) appeared to be severely distorted owing to variations in the *intra*-octahedral O1–Fe–O2 bond angles.
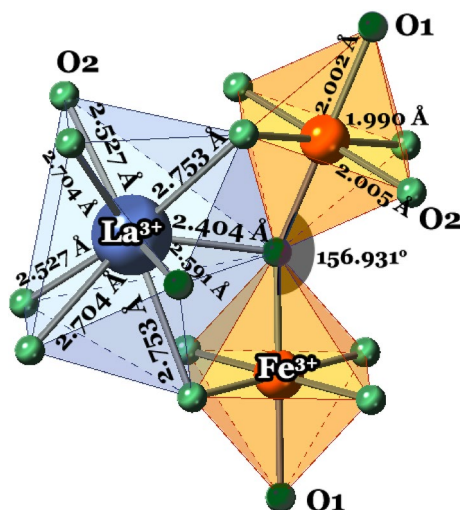
Figure 3. The polyhedra of the $LaFeO_3$ nanoparticles as derived from the XRD Rietveld refinement. The large gray spheres represent La^{3+} ions in 8 O^{2-} coordinated sites, the orange spheres refer to Fe^{3+} ions in FeO_6 octahedra and the small green spheres represent O^{2-} ions. O1 and O2 refer to O^{2-} ions with two different environments.

It is clear from the obtained lattice parameters of the $LaFeO_3$ nanoparticles that their distorted crystal structure is of the *O'-type*[6]. The diffraction peaks of the $La_{0.70}Eu_{0.30}FeO_3$ nanoparticles broadened and shifted toward larger angles (Fig. 1). Hence, their lattice constants decreased relative to those of the $LaFeO_3$ nanoparticles (Table 1). These changes entail the substitution of 8-coordinated La^{3+} ions (1.36 Å) with smaller 8-coordinated Eu^{3+} ions (1.066 Å) in the lattice structure of $LaFeO_3$[26]. Generally, the influence of the Eu^{3+} dopant on the deformation of octahedral sites is justifiable in terms of the Goldsmith formalism[7]. In contrast to the $LaFeO_3$ nanoparticles, it can be seen from Table 1 that doping with Eu^{3+} affects the lattice constants of the $La_{0.70}Eu_{0.30}FeO_3$ nanoparticles, such that $a < c/\sqrt{2} < b$ indicates that the orthorhombic distortion of the nanoparticles is *O-type*. We associate this crossover of the a and $c/\sqrt{2}$ parameters with the significant difference between the O1-Fe-O2 angle in the Eu^{3+}-doped $LaFeO_3$ nanoparticles and $LaFeO_3$ nanoparticles (Table 1) owing to the partial substitution of La^{3+} ions with smaller Eu^{3+} ions. Similar anomalous parameter crossovers have been reported for solid solutions of rare-earth orthoferrites and orthocobaltites, such as $PrCo_{1-x}Fe_xO_3$ and $EuCo_{1-x}Fe_xO_3$[27,28]. To reflect more on the structural distortion resulting from Eu^{3+} doping, using Glazer's tilt system of perovskites[29], one notes that the variation in the lattice parameters of the $La_{0.70}Eu_{0.30}FeO_3$ nanoparticles corresponds to the first tilt type along the [010] direction. As shown in Table 1, partial substitution of La^{3+} with Eu^{3+} led to a single long Fe-O2 bond along the b-axis and a pair of Fe-O1 and Fe-O2 short bonds in the ac plane.

We now turn to $La_{0.70}Eu_{0.30}Fe_{0.95}Cr_{0.05}O_3$ nanoparticles. As shown in Table 2, the Eu^{3+} and La^{3+} ions preferentially occupy a slightly distorted "average" A-site, whereas the Cr^{3+} ions are randomly distributed with Fe^{3+} ions in the B-sub-lattice.. It turns out that the introduction of 5% Cr^{3+} (0.615 Å) substituent ions for Fe^{3+} (0.645 Å)[26] resulted in a slight increase in the a lattice parameter and a concomitant decrease in the b and c lattice parameters relative to those of the $La_{0.70}Eu_{0.30}FeO_3$ nanoparticles. The estimated crystallite sizes for the three types of nanoparticles were within experimental error, consistent with the particle sizes deduced from the TEM measurements. This implies that the nanoparticles may generally be considered crystallites.

The FT-IR spectra of the mechano-synthesized $LaFeO_3$ nanoparticles and their Eu^{3+}-doped and Eu^{3+}/Cr^{3+}-co-doped modifications in the range of 400–700 cm^{-1} shown in Fig. 4 are typical of perovskite oxides that structurally index to the *Pbnm* space group[4,7]. Theoretically, *Pbnm* phases have nine dipole-active optical phonon modes in the 400–700 cm^{-1} range, of which those between 400 and 500 cm^{-1} are O^{2-} octahedral bending vibrations, and those beyond 500 cm^{-1} are O^{2-} stretching vibrations[7,30]. However, some peaks are very difficult to detect because of the line broadening associated with the small particle sizes or the possible presence of O^{2-} vacancies on the surfaces. Evidently, the slight differences in the FT-IR spectra relative to the spectrum of the $LaFeO_3$ nanoparticles were a consequence of cationic doping. On the basis of the ionic interactions present, the vibrational bands would contribute intrinsic Lorentzian shapes to the FT-IR spectrum. Temperature-dependent effects, instrumental effects, and/or sample characteristics cause the background signals to experience Gaussian broadening[31,32]. Hence, we opted to fit the FT-IR spectra shown in Fig. 4 with the Voigt functions. The spectral broadband at ~ 588 cm^{-1}, for the $LaFeO_3$ nanoparticles was assigned to the antisymmetric stretching vibrational modes of the FeO_6 octahedra[7]. The relatively asymmetric peak may be related to the non-uniform cationic distribution in the shells of the nanoparticles, which leads to cluster-glass-like features[14]. Peak broadening reflects the wide size distribution observed in the TEM image (Fig. 2). The weak band at *ca.* 505 cm^{-1} owing to the out-of-phase stretching vibrations of the BO_6 octahedra, as has been observed for some orthochromites and orthomanganites[32], is closely associated with a Jahn–Teller-like distortion[30]. For Eu^{3+}-and Eu^{3+}/Cr^{3+}-doped $LaFeO_3$ nanoparticles,

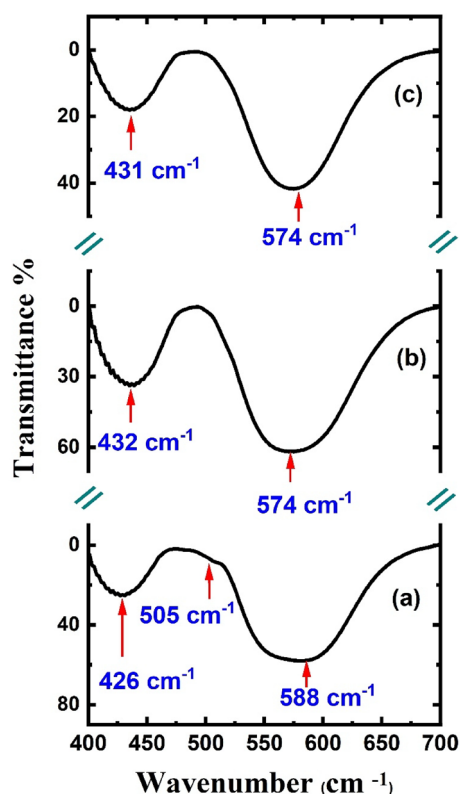**Figure 4.** FT-IR spectra of the (**a**) $LaFeO_3$, (**b**) $La_{0.70}Eu_{0.30}FeO_3$, and (**c**) $La_{0.70}Eu_{0.30}Fe_{0.95}Cr_{0.05}O_3$ nanoparticles in the range of 400–700 cm^{-1} at 298 K.

the notable enhancement in the symmetry of the stretching vibrational modes and their narrowing are indicative of a more uniform cationic distribution and limited particle size range relative to those of the $LaFeO_3$ nanoparticles. The substitution of the lighter La^{3+} ions (138.904 amu) by heavier Eu^{3+} ions (151.962 *amu*) in the $La_{0.70}Eu_{0.30}FeO_3$ nanoparticles shifted the absorption band of the FeO_6 stretching vibrations from 583 to 574 cm^{-1}, which is expected, as the wavenumber is inversely proportional to the ionic mass[18,33]. The small concentration of Cr^{3+} ions in the $La_{0.70}Eu_{0.30}Fe_{0.95}Cr_{0.05}O_3$ nanoparticles was not sufficient to cause an observable shift for the same band relative to that of the $La_{0.70}Eu_{0.30}FeO_3$ nanoparticles. The small shoulder at 505 cm^{-1}, associated with the *O′-type* structural mode of $LaFeO_3$ does not exist in the Eu^{3+}-doped and Eu^{3+}/Cr^{3+}-co-doped nanoparticles, presumably because of the *O-type* structural distortion. We now turn to The shifts in the bending vibrational mode at 426 cm^{-1} in the FT-IR spectrum of the $LaFeO_3$ nanoparticles to 432 cm^{-1} and 431 cm^{-1} in the spectra of $La_{0.70}Eu_{0.30}FeO_3$ and $La_{0.70}Eu_{0.30}Fe_{0.95}Cr_{0.05}O_3$, respectively. These shifts are consistent with the increased bending of the Fe–O2–Fe angle revealed by the XRD refinement of the $La_{0.70}Eu_{0.30}FeO_3$ nanoparticles and the subsequent decrease in the electronegativity of Cr^{3+}–O^{2-} compared with Fe^{3+}–O^{2-} in the $La_{0.70}Eu_{0.30}Fe_{0.95}Cr_{0.05}O_3$ nanoparticles. Hence, the FT-IR spectra further confirmed that $LaFeO_3$ nanoparticles and their Eu^{3+}-doped and Eu^{3+}/Cr^{3+} co-doped modifications were formed.

Mössbauer characterization

The zero-field ^{57}Fe Mössbauer spectra of $LaFeO_3$, $La_{0.70}Eu_{0.30}FeO_3$ and $La_{0.70}Eu_{0.30}Fe_{0.95}Cr_{0.05}O_3$ nanoparticles, recorded at 298 K and 78 K, are shown in Fig. 5, and the corresponding fitted hyperfine parameters are given in Table 3. All spectra show pure magnetic six-line patterns with broadened absorption lines, which reflect both the particle size distribution and varied cationic environments for the doped samples around the ^{57}Fe nuclei. It is pertinent to note that Fujii et al.[1] reported Mössbauer spectra for $LaFeO_3$ nanoparticles with an average particle size of *ca.* 13 nm, which are pure doublets. While the $LaFeO_3$ system is essentially AFM in character, the Mössbauer doublets were attributed to the superparamagnetic behavior of the FM nanoparticle shells that resulted from the uncompensated surface spins[1]. The absence of such doublets in the Mössbauer spectra of the present nanoparticles rules out the presence of any superparamagnetic behavior, which is consistent with their relatively larger average particle sizes relative to 13 nm[1,14]. The Mössbauer spectrum of the $LaFeO_3$ nanoparticles at either 298 or 78 K was best fitted to a single sextet with a typical isomer shift value of the Fe^{3+} state[11,34]. The isomer shift values at 298 K (0.37–0.41 mm/s) indicate the high-spin nature of the Fe^{3+} ions in all nanoparticles[6]. The increase in the isomer shift values at 78 K relative to their values at 298 K is explicable in terms of the second-order Doppler shift[34]. The small negative quadrupole shift values at both temperatures are indicative of the distorted crystal structures, as discussed earlier[6,11]. We associate the relatively high value of the hyperfine magnetic field of the $LaFeO_3$ sample at 298 K (51.5 T), which is typical for nanoparticles exhibiting
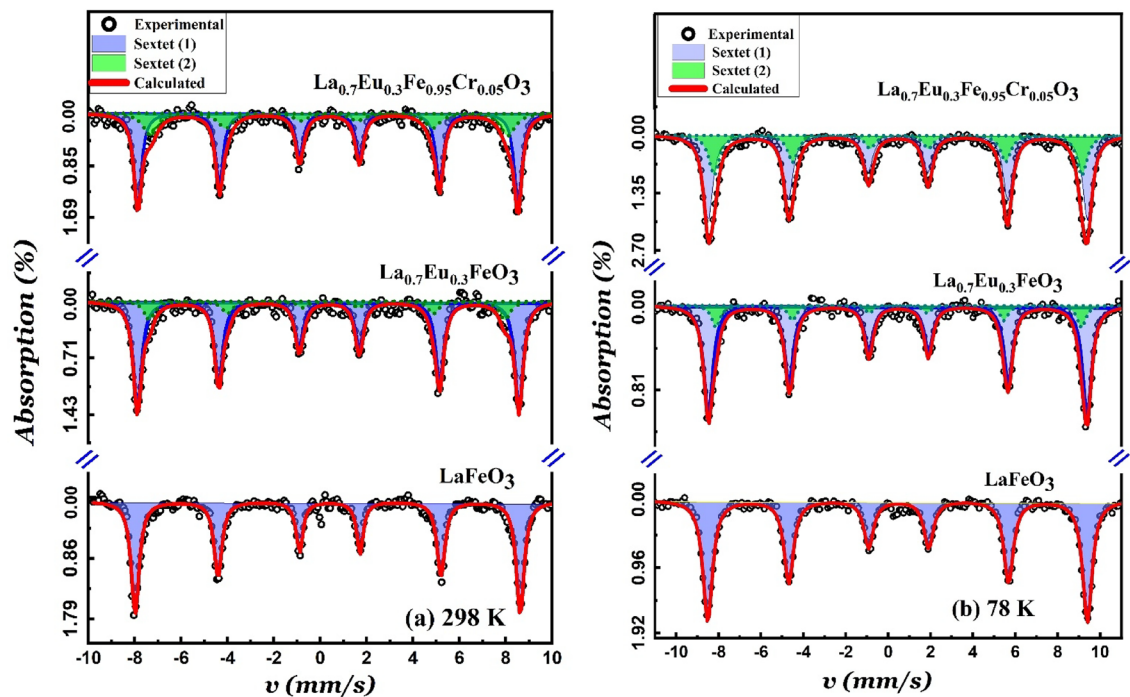
Figure 5. The ^{57}Fe Mössbauer spectra recorded from the (**a**) LaFeO$_3$, (**b**) La$_{0.70}$Eu$_{0.30}$FeO$_3$, and (**c**) La$_{0.70}$Eu$_{0.30}$Fe$_{0.95}$Cr$_{0.05}$O$_3$ nanoparticles at (**a**) 298 K and (**b**) 78 K.

	Sub-spectrum	δ (mms) ± 0.02	ε (mms) ± 0.02	H$_{eff}$ (T) ± 0.2	Area (%) ± 2
LaFeO$_3$	S	0.37(0.47)	−0.04(−0.03)	51.5(55.5)	100(100)
La$_{0.7}$Eu$_{0.3}$FeO$_3$	S1	0.37(0.47)	−0.02(−0.02)	51.0(55.3)	88(89)
	S2	0.38 (0.49)	−0.06 (0.00)	47.3(53.1)	12(11)
La$_{0.7}$Eu$_{0.3}$Fe$_{0.95}$Cr$_{0.05}$O$_3$	S1	0.37(0.47)	−0.03(−0.01)	50.7(55.2)	86(86)
	S2	0.41(0.50)	0.04(−0.03)	47.1(52.6)	14(14)

Table 3. The hyperfine parameters derived from fitting the Mössbauer spectra recorded at 298 K and 78 K (*between brackets and in italics*) for the LaFeO$_3$, La$_{0.70}$Eu$_{0.30}$FeO$_3$ and La$_{0.70}$Eu$_{0.30}$Fe$_{0.95}$Cr$_{0.05}$O$_3$ nanoparticles. *S* magnetic sextet, *δ* isomer shift, *ε* quadrupole shift, *H$_{eff}$* hyperfine magnetic field.

AFM ordering with strong Fe–Fe coupling, with Fe nuclei at the nanoparticle cores[1,6]. The tangible increase in the hyperfine field value as the temperature is decreased to 78 K (Table 3) is associated with the removal of the thermal vibrations and subsequent spin alignment, especially in the shells of the nanoparticles[1,13,15,34]. As shown in Fig. 5 and Table 3, doping the LaFeO$_3$ nanoparticles with Eu^{3+} and co-doping them with Eu^{3+}/Cr^{3+} broadened the Mössbauer absorption lines. The best fit of the spectra of both doped nanoparticles was attained using two superimposed magnetic subspectra, S1 and S2. S1, with smaller isomer shifts and larger effective hyperfine magnetic fields, are associated with Fe^{3+} environments similar to those in undoped LaFeO$_3$ or with poor Eu^{3+} (in La$_{0.70}$Eu$_{0.30}$FeO$_3$) and Eu^{3+}/Cr^{3+} (in La$_{0.70}$Eu$_{0.30}$Fe$_{0.95}$Cr$_{0.05}$O$_3$) environments. The slight decrease in the hyperfine field values of sextet S1 at both temperatures for both types of doped nanoparticles relative to those of the LaFeO$_3$ nanoparticles is attributed to their relatively smaller average particle size, as revealed by the TEM images. Slight differences existed between the isomer shift values of the undoped LaFeO$_3$ nanoparticles and those of the S1 sextet. This may be related to the different electronic configurations of the dopant ions that, in turn, lead to slightly different electric fields at the sites of ^{57}Fe nuclei[34]. Sextet S2, whose hyperfine magnetic fields are notably smaller than those of the LaFeO$_3$ nanoparticles, is associated with Fe^{3+} environments where the Fe–O–Fe of the magnetic superexchange interaction of pristine LaFeO$_3$ is weakened by the presence of Eu^{3+} or Eu^{3+}/Cr^{3+} nearest neighbors in La$_{0.70}$Eu$_{0.30}$FeO$_3$ or La$_{0.70}$Eu$_{0.30}$Fe$_{0.95}$Cr$_{0.05}$O$_3$, respectively. This is supported by the larger linewidth of S2 for the La$_{0.70}$Eu$_{0.30}$Fe$_{0.95}$Cr$_{0.05}$O$_3$ nanoparticles, which, in turn, suggests a random distribution in the numbers of Eu^{3+} and Cr^{3+} cationic neighbors of the Fe^{3+} ions at the A and B sites, respectively[6,34]. The weakening of the S1 and S2 hyperfine magnetic fields in the spectra of the La$_{0.70}$Eu$_{0.30}$Fe$_{0.95}$Cr$_{0.05}$O$_3$ nanoparticles implies weakened exchange interactions between Fe^{3+} ions because of the negative super-transferred hyperfine field produced by the half-filled d-orbitals of the Cr^{3+} ions at the sites of the ^{57}Fe nuclei[35]. The fact that the spectral intensities at

298 K and 78 K for both sextets, S1 and S2, are the same supports their assignments to the Fe^{3+} environments, as described above.

Surface composition: XPS spectral analysis

The La 3d, Eu 3d, Fe 2p and O1s XPS spectra of the $LaFeO_3$ nanoparticles and their Eu^{3+}-doped and Eu^{3+}/Cr^{3+} co-doped modifications are shown in Fig. 6. The C 1s XPS peak at 284.6 eV was taken as a reference for all charge shift corrections. The La $3d_{3/2}$ and La $3d_{5/2}$ peaks of the $LaFeO_3$ sample at the binding energies (BE) 850.4 eV and 833.6 eV (Fig. 6a) are similar to those reported for sol–gel processed $LaFeO_3$ nanoparticles[7,36]. Satellite peaks at BE values 854.4 eV and 837.3 eV correspond to the shake-up of the La $3d_{3/2}$ and La $3d_{5/2}$ states, respectively, due to electron transfer from the O 2p valence band to empty La 4f states[36]. As these BE values have been reported for both La_2O_3 and $LaFeO_3$[7,37], the existence of some unreacted La_2O_3 components on the surface of these mechano-synthesized $LaFeO_3$ nanoparticles could not be ruled out. Additionally, these BE values may be partly associated with the very small amounts of Fe-doped La_2O_3[38] and/or La-doped α-Fe_2O_3[39] intermediate phases that develop during the reaction, leading to the $LaFeO_3$ phase. The BE values of the La $3d_{3/2}$ and La $3d_{5/2}$ spectra for the $La_{0.70}Eu_{0.30}FeO_3$ nanoparticles, 850.8 eV and 834.0 eV, and those of the $La_{0.70}Eu_{0.30}Fe_{0.95}Cr_{0.05}O_3$ nanoparticles, 849.9 eV and 833.1 eV, are slightly higher than those of the $LaFeO_3$ nanoparticles. This implies that introducing the more electronegative Eu^{3+} (1.2) for the less electronegative La^{3+} (1.1) shifts the La 3d spectral peaks towards higher BE values because of the lowering of the electron densities[40]. Similarly, the lower BE values for the La 3d spectral peaks of the $La_{0.70}Eu_{0.30}Fe_{0.95}Cr_{0.05}O_3$ nanoparticles relative to those of the $La_{0.70}Eu_{0.30}FeO_3$ nanoparticles may be attributed to doping with the less electronegative Cr^{3+}(1.66) for the more electronegative Fe^{3+} (1.83), which increases the La^{3+} and O^{2-} electron densities and consequently lowers the BE values[40].
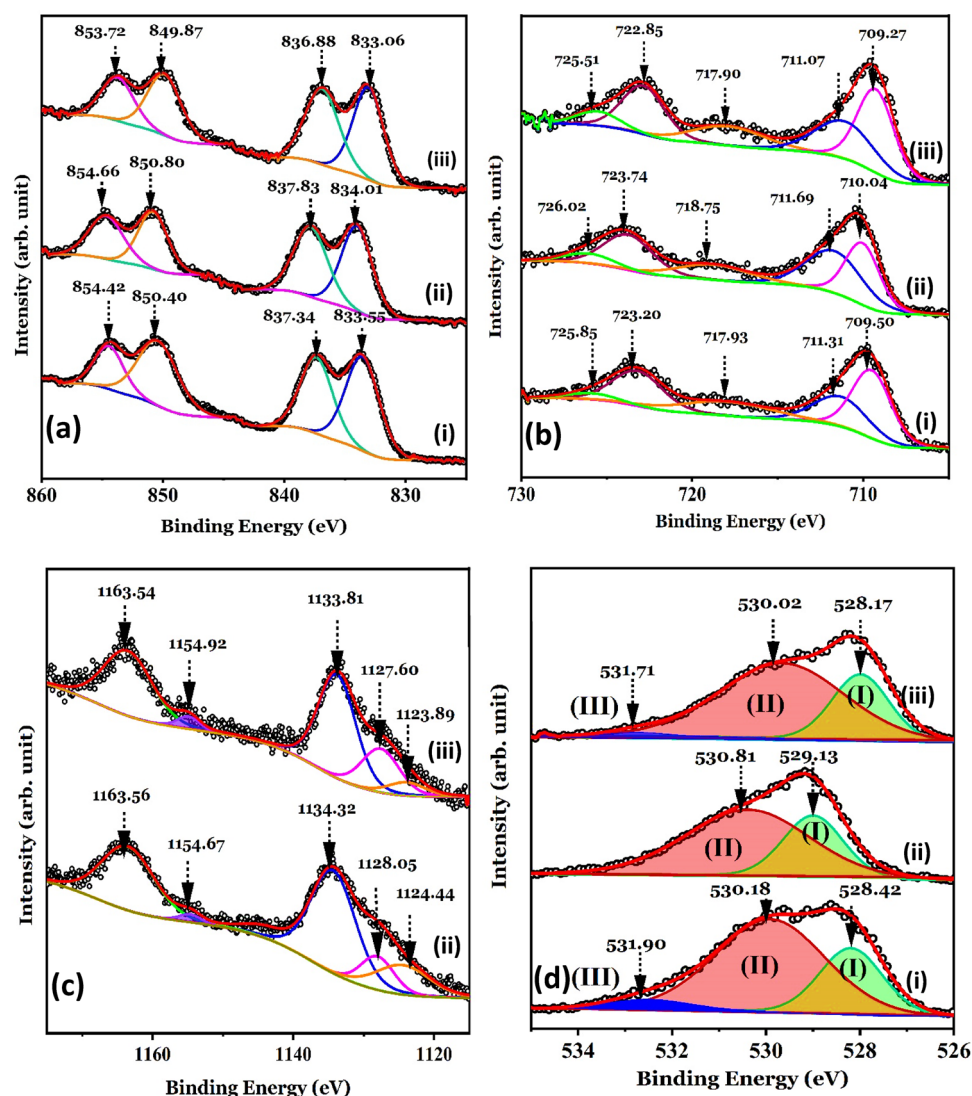

Figure 6. The (**a**) Fe 2p, (**b**) La 3d, (**c**) Eu 3d, and (**d**) O 1s core-level XPS spectra recorded from the (i) $LaFeO_3$, (ii) $La_{0.70}Eu_{0.30}FeO_3$, and (iii) $La_{0.70}Eu_{0.30}Fe_{0.95}Cr_{0.05}O_3$ nanoparticles. The solid lines represent the best fitting of the experimental data. The estimated error for the binding energy values is ± 0.01 eV.

Figure [6]b shows the Fe 2p XPS spectra of all the nanoparticles. The asymmetrical Fe $2p_{3/2}$ peak of the $LaFeO_3$ nanoparticles could be decomposed into distinct peaks at BE of 709.5 eV and 711.3 eV corresponding, respectively, to surface Fe^{2+}- and Fe^{3+}-containing species[7,41]. Previously, we reported a similar reduction of Fe^{3+} to Fe^{2+} on the surface of mechano-synthesized $Nd_{0.33}Eu_{0.67}Cr_xFe_{1-x}O_3$ nanoparticles[15]. In addition, the presence of surface Fe^{2+} ions has been reported for other $REFeO_3$ compounds in the form of bulk or nanoparticles, such as $PrFeO_3$[42], $ErFeO_3$[43] and Ir-doped $YbFeO_3$[44]. In fact, the shake-up satellite peak at a BE value of 717.8 eV, which is located at +8.3 eV from the Fe $2p_{3/2}$ peak at 709.5 eV, is typical of satellite signals of ferrous species[41]. The presence of these Fe^{2+} impurities suggests the existence of O^{2-} vacancies as balancing defects. Together, these results imply the formation of an O^{2-} defective perovskite phase of $LaFeO_{3-\delta}$ at the surface of the nanoparticles[45]. Hence, we associate the Fe $2p_{3/2}$ peak at the BE of 709.5 eV to this surface $LaFeO_{3-\delta}$ component. The sub-spectral peak at 711.3 eV is almost similar to that of Fe^{3+} ions in α-Fe_2O_3 (711.2 eV). Hence, we associate the 711.3 eV peak with the La-doped α-Fe_2O_3 intermediate phase implied above by the La 3d XPS spectrum[39]. The Fe $2p_{1/2}$ spectral component was fitted with two peaks centered at the BE values of 723.2 eV and 725.8 eV which are assigned, respectively, to $LaFeO_{3-\delta}$ and either or both of $LaFeO_3$ and La-doped α-Fe_2O_3[7,36,39]. As is seen in Fig. [6]b, the binding energies of the Fe $2p_{3/2}$ peaks increase for the $La_{0.70}Eu_{0.30}FeO_3$ nanoparticles (710.0, 711.7 eV) relative to the corresponding values of the $LaFeO_3$ nanoparticles. This is suggestive that the incorporation of Eu^{3+} in $LaFeO_3$ results in lesser O^{2-} vacancies hence more Fe^{3+} ions and, consequently, stronger Fe–O bonds. However, for the $La_{0.70}Eu_{0.30}Fe_{0.95}Cr_{0.05}O_3$ nanoparticles the binding energies of Fe 2p core-level spectra tend to decrease on the Cr^{3+} substitution. The reason for this is apparently the same as that we argued above for the similar trend in the La 3d spectra following the Cr^{3+} substitution.

Each of the Eu 3d core-level XPS spectra of the Eu^{3+}-doped and Eu^{3+}/Cr^{3+}-co-doped $LaFeO_3$ nanoparticles, shown in Fig. [6]c, is composed of five peaks. For the $La_{0.70}Eu_{0.30}FeO_3$ sample, the peaks were assigned as follows. The Eu^{3+} doublet at the BE values of 1134.3 eV (Eu $3d_{5/2}$) and 1163.6 eV (Eu $3d_{3/2}$) is attributed to a surface Eu^{3+}-doped α-Fe_2O_3, as is reported elsewhere[46]. The weak Eu^{2+} doublet at the BE values 1124.4 eV (Eu $3d_{5/2}$) and 1154.7 eV (Eu $3d_{3/2}$), which is consistent with those reported before for other Eu-containing systems[47], merits special attention as it appears to influence the nanoparticles' low temperature magnetic behavior to be discussed in the next section. The presence of Eu^{2+} ions, in systems like the present ones, is attributed to an intermediate valence between the electronic configurations of Eu^{3+} and Eu^{2+} ions[48]. This reduction of Eu^{3+} to Eu^{2+} is implicative of the presence of balancing O^{2-} vacancies on the surface of nanoparticles. Hence, we associate the Eu^{2+} doublet with the weak $La_{0.7}Eu_{0.3}FeO_{3-\delta}$ surface component. The fifth fitted peak in the Eu 3d core level spectrum, at the BE value 1128.1 eV was not, to our knowledge, reported before for any Eu-containing solid. Hence, we assume that it is due to the investigated $La_{0.70}Eu_{0.30}FeO_3$ nanoparticles. Such an assignment appears logical as the Eu 3d core level XPS spectral peak at the close BE value of 1129.0 eV was assigned before to $Nd_{0.33}Eu_{0.67}FeO_3$ nanoparticles[15].

As is clear from Fig. [6]c, the presence of Cr^{3+} in the $La_{0.70}Eu_{0.30}Fe_{0.95}Cr_{0.05}O_3$ nanoparticles slightly shifts the Eu 3d doublet relative to that of the $La_{0.70}Eu_{0.30}FeO_3$, to the BE values of 1133.8 eV and 1163.5 eV. These values are consistent with those reported for $EuCrO_3$ doublets, suggesting the possibility that traces of $EuCrO_3$ are present on the surface of $La_{0.70}Eu_{0.30}Fe_{0.95}Cr_{0.05}O_3$ nanoparticles[25]. In similar lines to those given above, we attribute the Eu 3d core-level XPS peak at the BE value 1123.9 eV and the shake-down satellite at 1154.9 eV, in the spectrum of the $La_{0.70}Eu_{0.30}Fe_{0.95}Cr_{0.05}O_3$ nanoparticles, to an Eu^{2+}-containing surface component that could be $La_{0.7}Eu_{0.3}FeO_{3-\delta}$ and/or $La_{0.70}Eu_{0.30}Fe_{0.95}Cr_{0.05}O_{3-\delta}$[47]. The fifth peak in the Eu 3d spectrum of the same sample, at the BE value of 1127.6 eV, is negatively shifted and enhanced in intensity relative to the corresponding one in the spectrum of $La_{0.70}Eu_{0.30}FeO_3$. Taken together, these results imply that even a low concentration of the less electronegative Cr^{3+} relative to the substituted Fe^{3+} may significantly influence the surface composition of the mechano-synthesized $La_{0.70}Eu_{0.30}Fe_{0.95}Cr_{0.05}O_3$ nanoparticles, with the possibility of having surface traces of pure and/or Cr^{3+}-doped $La_{0.70}Eu_{0.30}FeO_{3-\delta}$ as well as $EuCrO_3$[25].

The O 1s XPS spectra of the nanoparticles are shown in Fig. [6]d. As we have, previously, done with similarly mechano-synthesized rare earth orthoferrites[15], we resolve the O 1s peak for the $LaFeO_3$ nanoparticles into three overlapping peaks. In agreement with the La 3d spectra, the first component of the O 1s peak (I) at a BE value of 528.2 eV is related to perovskite-related $LaFeO_3$ and/or moderately Fe-doped La_2O_3[7,36,38]. The second component (II) at 529.9 eV is assigned to the α-Fe_2O_3 and/or La-doped α-Fe_2O_3, both of which are implicated by the Fe 2p spectra discussed above[15,39,41]. The $LaFeO_{3-\delta}$ phase, whose presence was inferred from the Fe 2p spectra, is associated with the minor third component of O 1s (III) at the BE value of 532.5 eV[15,41,45]. With Eu^{3+} doping, the BE of the components of the O 1s peak increased to 529.0 eV (I) and 530.4 (II) eV which, in line with the above analysis, we ascribe to $La_{0.70}Eu_{0.30}FeO_3$ and Eu^{3+}-doped α-Fe_2O_3, respectively[46]. The positive shift of O 1s, in the XPS $La_{0.70}Eu_{0.30}FeO_3$ spectrum, is possibly due to the decrease in the distance between the O^{2-} ion and their doped Eu^{3+} neighbors due to the higher electronegativity of Eu^{3+} relative to that of La^{3+}[40]. The absence of the third component (III) in the O 1s XPS spectrum of the $La_{0.70}Eu_{0.30}FeO_3$ sample suggests that doping with Eu^{3+} results in the elimination of the Fe^{2+}-containing $LaFeO_{3-\delta}$ surface component. With the inclusion of the Cr^{3+} ion, the BE values of the three O 1s XPS peaks decrease slightly to 528.0 eV (I), 529.6 eV (II) and 532.7 eV (III) relative to those of the $La_{0.70}Eu_{0.30}FeO_3$ nanoparticles. Such a reduction is attributed to the lower electronegativity[40] of Cr^{3+} over Fe^{3+}. Based on previous work, and in line with above analysis, the BE values of these O 1s XPS spectral peaks are assigned, respectively to $EuCrO_3$, Eu^{3+}-doped α-Fe_2O_3 and pure and/or Cr^{3+}-doped $La_{0.70}Eu_{0.30}FeO_{3-\delta}$ surface components[25]. To summarize, the above XPS data analysis has shown mechano-synthesized Eu^{3+}-doped and Eu^{3+}/Cr^{3+}-co-doped $LaFeO_3$ nanoparticles to have complex surface structures, that contain pure and Eu^{3+}/Cr^{3+} doped and co-doped $LaFeO_3$ phases, O^{2-}-deficient undoped and Eu^{3+}/Cr^{3+}-doped $LaFeO_3$ phases, traces of undoped or doped initial reactants. Such complexity is expected on the surfaces of nanoparticles prepared by mechanical milling and subsequent sintering[15,25].

The magnetic properties

Figure 7 shows the temperature dependence of the FC and ZFC magnetization in the range of 2–300 K under an applied field of 50 kOe for LaFeO$_3$, Eu^{3+}-doped, and Eu^{3+}/Cr^{3+}-co-doped LaFeO$_3$ nanoparticles. As expected for a magnetically ordered system, the FC magnetization curves for all samples exhibited similar temperature dependencies to their Mössbauer magnetic hyperfine fields, decreasing with increasing temperature. The wider bifurcation observed for the LaFeO$_3$ nanoparticles reveals stronger thermomagnetic irreversibility in comparison to the Eu^{3+}-doped and Eu^{3+}/Cr^{3+}-co-doped nanoparticles[13]. The ZFC magnetization of the LaFeO$_3$ nanoparticles initially decreased with decreasing temperature to a minimum and then increased without exhibiting a clear maximum below the bifurcation point[49]. Based on the Mössbauer data, this could be explained in terms of the core/shell model, as was done by other[1,13,16,49] researchers. While the core is AFM in nature, the spins of the glass-like shells assume an FM ordering owing to the AFM spin canting at the cores in addition to the field applied during the measurement. The magnetization enhancement to values similar to those previously reported for LaFeO$_3$ nanoparticles at very low temperatures could result from a local spin order that develops at the interface between the canted AFM cores and FM shells as a result of strong spin coupling[9,13,50]. With a gradual increase in temperature, the interfacial exchange coupling weakens, while the core spins resist alignment even by a field as high as 50 kOe[50]. Thus, the core–shell AFM-FM coupling requires higher thermal agitation and/or a higher applied field to be weakened, as manifested by the development of the spin-glass-like behavior at ~ 75 K (Fig. 7). This may explain why spin-glass-like behavior was not detected by zero-field Mössbauer measurements at 78 K. At temperatures higher than 75 K, the spins of the FM shell start to reverse their orientation in the direction of the applied field, and concomitantly, the AFM coupling at the cores starts to decay. Consequently, the ZFC magnetization increased with a further increase in temperature, as observed[9,10]. Similar behavior was not observed in the FC curve of the same sample because the surface spins were readily aligned in the field direction, resulting in an apparently higher magnetization relative to that obtained in the ZFC case (Fig. 7).

As shown in Fig. 7, with decreasing temperature, the ZFC and FC magnetization values for the La$_{0.70}$Eu$_{0.30}$FeO$_3$ and La$_{0.70}$Eu$_{0.30}$Fe$_{0.95}$Cr$_{0.05}$O$_3$ nanoparticles increased throughout the scanned temperature range. The higher magnetization values for both materials relative to those of the pristine LaFeO$_3$ sample are evidently linked to the introduction of paramagnetic Eu ions as partial substituents for diamagnetic La^{3+}. A comparison of the FC molar susceptibility (χ_m) values of the three materials, as depicted in Fig. 8, reveals that the magnetic contribution of the Fe^{3+} ions is barely detectable in LaFeO$_3$ compared to that of the Eu ions in the other two compounds. To determine the contribution of Eu^{3+} and XPS-detected minority surface Eu^{2+} ions to the total susceptibility of both the Eu-doped samples, hereafter referred to as χ_m(Eu), we subtracted χ_m of the LaFeO$_3$ from that of either. The rationale here is to exclude the magnetic effect of the Fe^{3+} sublattice, which is similar in all three compounds. Each of the obtained χ_m(Eu) curves, shown in Fig. 9a (La$_{0.70}$Eu$_{0.30}$FeO$_3$) and 9-b (La$_{0.70}$Eu$_{0.30}$Fe$_{0.95}$Cr$_{0.05}$O$_3$), may be divided into two temperature regions, viz. 2–20 K and 20–300 K. In the first low temperature region, the observed upward ascending trend of χ_m(Eu) below 20 K is implicative of a Curie–Weiss type paramagnetism that is solely associated with the minority Eu^{2+} ions having an electronic configuration of [Xe] 4f^7 and a theoretical effective magnetic moment μ_{eff} of 7.94 μ_B similar[48] to that of Gd^{3+}. In the second region, the behavior of χ_m(Eu) was attributed *mainly* to the van Vleck paramagnetism of the Eu^{3+} excited states[48]. According to the Russell–Saunders formalism, Eu^{3+} ([Xe] 4f^6) has a total angular momentum (J) of zero and, hence, a nonmagnetic ground state ($^7F_0$)[53]. Nevertheless, Eu^{3+} has a spin–orbit interaction given by ($\lambda L.S$) with L and S orbital and spin angular momenta,
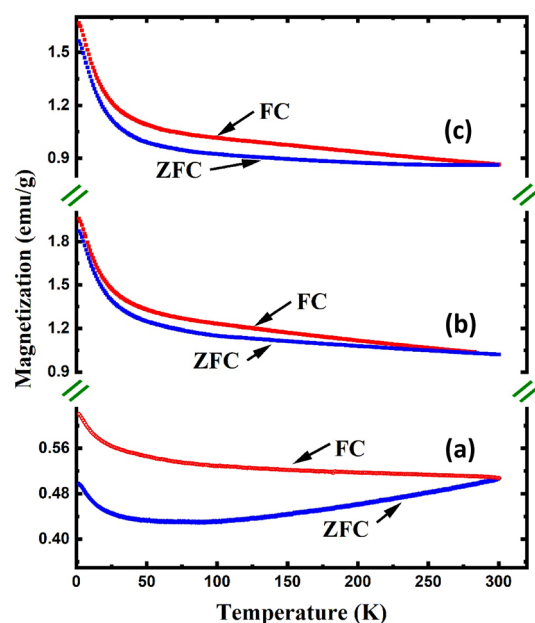

Figure 7. The temperature dependence of the FC and ZFC magnetization of the (**a**) LaFeO$_3$, (**b**) La$_{0.70}$Eu$_{0.30}$FeO$_3$, and (**c**) La$_{0.70}$Eu$_{0.30}$Fe$_{0.95}$Cr$_{0.05}$O$_3$ nanoparticles under an applied field of 50 kOe.
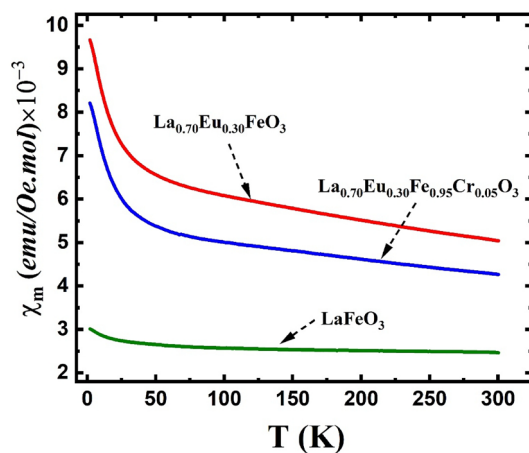
Figure 8. Temperature dependence of magnetic molar susceptibility for the $LaFeO_3$, $La_{0.70}Eu_{0.30}FeO_3$ and $La_{0.70}Eu_{0.30}Fe_{0.95}Cr_{0.05}O_3$ nanoparticles under an applied field of 50 kOe.
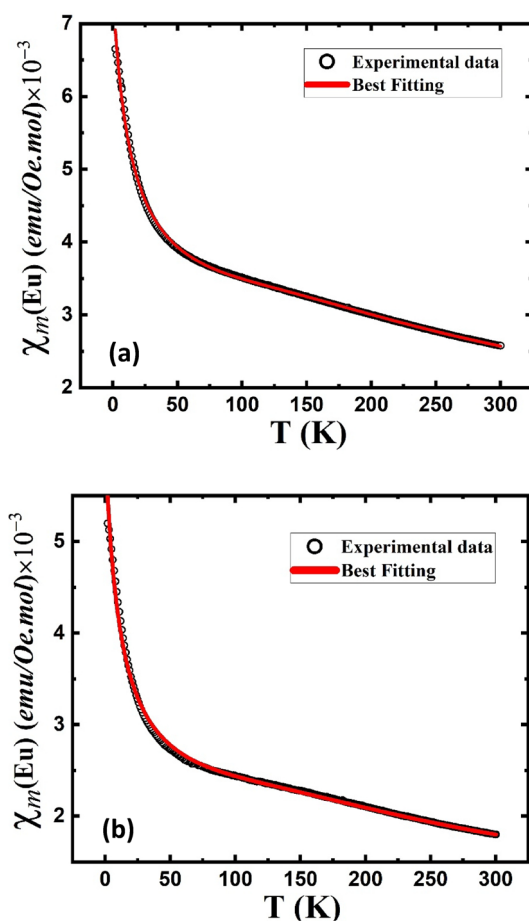

Figure 9. Temperature dependence of the FC Eu-related molar susceptibility χ_m (Eu) for the (**a**) $La_{0.70}Eu_{0.30}FeO_3$ and (**b**) $La_{0.70}Eu_{0.30}Fe_{0.95}Cr_{0.05}O_3$ nanoparticles, obtained by subtracting the molar susceptibility contribution of the $LaFeO_3$ nanoparticles from that of the $La_{0.70}Eu_{0.30}FeO_3$ and $La_{0.70}Eu_{0.30}FeO_3$ ones, respectively, measured in an applied field of 50 kOe. The solid line represents the best fitting line based on Eqs. (1) and (2).

respectively, and (λ) is the spin–orbit coupling constant[47,48,50]. In the framework of the van Vleck theory, the fact that the differences between the ground state and the low-lying excited states ^7F_J of the Eu^{3+} ion are of the order of k_BT at room temperature (207 cm^{-1}) results in the Eu^{3+} ions contributing a temperature-dependent term (χ) to the paramagnetic susceptibility, whose value depends on λ[48]. For instance, while for insufficiently large values of λ relative to (207 cm^{-1}), a non-negligible magnetic moment might be observed at low temperatures, the Eu^{3+} ions contribute a minute van Vleck temperature-independent paramagnetic term (χ_0) that is linked to the $^7F_0$ state[48]. Based on the above, the χ_m(Eu) curves in Fig. 9a,b were not amenable to satisfactory fits by separately applying a Curie–Weiss type equation to the low-temperature data and a van Vleck type equation fit to the data in the ~ 20–300 K temperature range. However, the best fits of each of the χ_m(Eu) curves in the entire temperature range of 2–300 K were obtained by considering both the temperature-independent and-dependent Eu^{3+} van Vleck terms in addition to the Eu^{2+} Curie–Weiss type paramagnetic term using the following equation[48]:

$$\chi_m(Eu) = \chi_o + n\chi_m(Eu^{2+}) + (1-n)\chi_m(Eu^{3+}) \tag{1}$$

where n is the relative Eu^{2+} contribution to the total χ_m(Eu) in the temperature range of the measurement. By limiting ourselves to the first three excited states of Eu^{3+}, Eq. (1) can be rewritten as follows:

$$\chi_m(Eu) = \chi_0 + n \times \frac{C}{T-\theta_W} + (1-n) \times \frac{N_A \mu_B^2}{3k_B T}$$
$$\times \frac{(24/a) + (13.5-1.5)e^{-a} + (67.5-2.5)e^{-3a} + (189-3.5)e^{-6a}}{1 + 3e^{-a} + 5e^{-3a} + 7e^{-6a}} \tag{2}$$

where N_A is Avogadro's constant, θ_W is the Weiss temperature, $a = \lambda/k_B T$. The other symbols have the usual meanings. This has yielded for the $La_{0.70}Eu_{0.30}FeO_3$ nanoparticles the values of $\mu_{eff} = 0.72\mu_B$, $\theta_W \sim -14$ K, $n = 0.58$, $\lambda = 363$ cm^{-1} and $\chi_0 = 5.3 \times 10^{-5}$ emu/Oe. mol. Similar values were obtained for the $La_{0.70}Eu_{0.30}Fe_{0.95}Cr_{0.05}O_3$ except for n and θ_W, which were found to be = 0.70 and ~ − 11 K, respectively. Starting with the low-temperature upturn in χ_m(Eu) that we ascribed to Eu^{2+} spins, it is evident that the negative values of θ_W imply the presence of AFM interactions among the Eu^{2+} spins. However, the obtained θ_W values for both compounds reflect the nature of this weak AFM interaction. The value of $\mu_{eff} = 0.72\mu_B/Eu^{2+}$ is very small when compared to the corresponding theoretical value for a free Eu^{2+} ion (7.94 μB)[50]. This could possibly reflect the fact that the Eu ions in both materials were in a valence fluctuation state with no localized magnetic moments. We now turn to the remaining part of the scanned temperature range, where the obtained value of λ suggests that the energy interval between the ground state ($^7F_0$) and first excited ($^7F_1$) state for $Eu^{3+}(4f^6)$ ions, in both compounds, primarily influences the paramagnetic susceptibility above 521 K. This, in turn, explains the weak relative contribution of the Eu^{3+} van Vleck temperature-dependent susceptibility to the total χ_m(Eu), viz. 0.42 ($La_{0.70}Eu_{0.30}FeO_3$) and 0.30 ($La_{0.70}Eu_{0.30}Fe_{0.95}Cr_{0.05}O_3$) in the 20–300 K temperature range. The fact that these results are slightly different from those reported for other Eu-containing oxide systems[48] could possibly be ascribed to the high applied field (H = 50 kOe), crystal field anisotropy of the distorted crystal structure, and screening effect, as indicated by the increase in the Mössbauer isomer shift of the S2 sextet (Table 3).

Figure 10 shows that the magnetization values of the $La_{0.70}Eu_{0.30}Fe_{0.95}Cr_{0.05}O_3$ nanoparticles were lower than those of the $La_{0.70}Eu_{0.30}FeO_3$ nanoparticles. This is presumably due to the substitution of the weaker magnetic Cr^{3+} ion (μ = 3 μB) for the stronger Fe^{3+} ion (μ = 5 μB), which weakens the AFM coupling relative to that of the $La_{0.70}Eu_{0.30}FeO_3$ nanoparticles[13,51]. The slight increase in the bifurcation of the $La_{0.70}Eu_{0.30}Fe_{0.95}Cr_{0.05}O_3$ nanoparticles relative to that of the $La_{0.70}Eu_{0.30}FeO_3$ nanoparticles can be attributed to an increased interface anisotropy caused by co-doping with both Eu^{3+} and Cr^{3+} ions. Considering the limited temperature range used for the FC and ZFC scans, we conclude this section by qualitatively commenting on the irreversibility temperature (T_{irr}) of the nanoparticles (Fig. 7). The value of T_{irr} for $La_{0.70}Eu_{0.30}FeO_3$, ~ 287 K, is lower than the corresponding values for the undoped and Eu^{3+}/Cr^{3+}-co-doped $LaFeO_3$ counterparts, both of which could not be determined firmly in the scanned temperature range. The reduction in T_{irr} for the $La_{0.70}Eu_{0.30}FeO_3$ sample relative to that of the $LaFeO_3$ sample can be explained using the argument given above for the enhancement of the ZFC magnetization values to approach those of the FC magnetization owing to doping with Eu^{3+}. Similarly, the higher T_{irr} of the $La_{0.70}Eu_{0.30}Fe_{0.95}Cr_{0.05}O_3$ nanoparticles relative to that of the $La_{0.70}Eu_{0.30}FeO_3$ nanoparticles is associated with the diminution of the ZFC magnetization values relative to those of the FC, following the introduction of Cr^{3+} ions.

A final comment in this part goes for the high applied field of 50 kOe used in the FC and ZFC measurements of Fig. 7 and the discussion that followed. This is exactly the same applied field value, deemed necessary to saturate the canted ferromagnetic moments of Fe^{3+}, by Ahmadvand et al.[49] in investigating the exchange bias effect in the pristine $LaFeO_3$. This is why it was easy to exclude the contribution of the Fe^{3+} moments in the above calculations of molar susceptibility. This spin canting arises from the disturbing effect of the crystalline field on the much stronger exchange field, as evidenced by hysteresis loops. Fitting the thermal-dependent magnetization at high field (1.5 kOe ≤ H ≤ 50 kOe) and low temperatures with the Curie–Weiss law, the saturation magnetization almost exclusively represents the rare earth moment, as found in[52].

To gain insight into the static features of the magnetic behavior in the three samples, temperature-dependent DC magnetization was performed under an applied field of 100 Oe, as shown in Fig. S1. One notices two distinct glassy states to emerge at ~ 93 K and ~ 90 K for the $LaFeO_3$ nanoparticles, that shift slightly to ~ 92 K and ~ 84 K for both the Eu^{3+} doped and Eu^{3+}/Cr^{3+} co-doped variants. This behavior may be linked to the magnetic anisotropy associated with the formation of short-range ordered ferromagnetic clusters and/or a strain-related spin reorientation process for the surface Fe^{3+} cations[53].

The ZFC hysteresis loops of the $LaFeO_3$, $La_{0.70}Eu_{0.30}FeO_3$ and $La_{0.70}Eu_{0.30}Fe_{0.95}Cr_{0.05}O_3$ nanoparticles were measured at 300 K, 200 K, 100 K and 4 K under an applied field (H) varying between − 9 T and 9 T. Only the
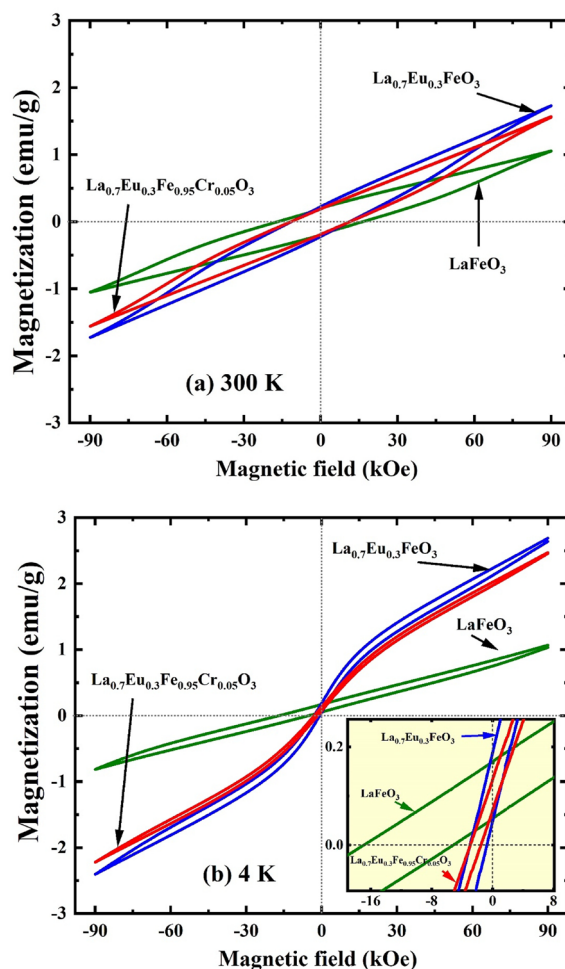
Figure 10. The hysteresis loops (M–H curves) of the LaFeO$_3$, La$_{0.70}$Eu$_{0.30}$FeO$_3$, and La$_{0.70}$Eu$_{0.30}$Fe$_{0.95}$Cr$_{0.05}$O$_3$ nanoparticles at (**a**) 300 K and (**b**) 4 K. The inset shows a zoom-in image of the same loops to display the non-zero values of both coercivity and remnant magnetization at 2 K.

loops measured at 300 K and 4 K are shown in Fig. 10. Generally, the loops exhibit a superposition of a dominant contribution ascribed to the AFM core and an FM contribution stemming from both the uncompensated spin-glass shell and canted AFM spins at the core[2,11,13,16,19]. The values inferred from Fig. 10 for some of the magnetic parameters are listed in Table 4[2]. The fact that a field as high as 9 T is not sufficient to saturate M at all temperatures indicates the dominant AFM behavior of the cores. Moreover, the hysteresis loops of the Eu-containing nanoparticles at 4 K, as compared to the pristine sample, exhibit a linear non-compensated paramagnetic contribution as well as a weak ferromagnetic behavior, as shown in the inset of Fig. 10b. The paramagnetic behavior is obviously due to the Curie Weiss-like behavior that was attributed to the surface Eu^{2+} ions at low temperatures in the preceding section. The small remnant magnetization (FM contribution) is due to the canted tendency of the FeO$_6$ octahedra, which affects the superexchange of neighboring Fe t$_{2g}$ electrons through Dzyaloshinskii–Moriya (DM) interactions[19,50]. The values of the instantaneous magnetization in the different M-H isotherms follow similar trends to those obtained for the FC magnetization of the nanoparticles (Fig. 8), such that La$_{0.70}$Eu$_{0.30}$FeO$_3$ has the highest M values and LaFeO$_3$ has the lowest magnetoelectric coupling in these multiferroic nanoparticles, which reduces the effective magnetic anisotropy[54].

While the values of M_{max} for the doped nanoparticles decreased with increasing temperature, as expected (Fig. 11a), for the LaFeO$_3$ nanoparticles, M_{max} was almost constant in all hysteresis isotherms. This is explicable in terms of the weakening of the exchange coupling of the spins at the AFM/FM core/shell interface, as suggested above, to enhance the ZFC magnetization of the same nanoparticles with temperature. Consequently, under the same maximum applied field (9 T), M_{max} was expected to be constant. The values derived from Fig. 10 for the coercivity H_c ($= (H_{c1} - H_{c2})/2$), where H_{c1} and H_{c2} are the coercive fields to the right and left of $H = 0$ values, are given in Table 4. Clearly, the doped samples had smaller H_c values relative to the LaFeO$_3$ nanoparticles. This may be partly explained in terms of the Stoner-Wohlfarth model, which relates the reduction in H_c to a corresponding reduction in magnetocrystalline anisotropy[55]. The smaller average particle sizes of the doped nanoparticles relative to those of the LaFeO$_3$ ones enhance the influence of the uncompensated surface spins that become susceptible to easy flipping by the applied field, thereby reducing H_c. It is interesting to note from

		M_{max} (emu/g) $[\mu_B$/f.u.]	$|H_c|$ (kOe)	$|EB|$ (Oe)
$LaFeO_3$	300 K	1.055(7) [0.05]	16.580(3)	216.650(3)
$La_{0.70}Eu_{0.30}FeO_3$		1.733(3) [0.08]	11.361(1)	77.900(1)
$La_{0.70}Eu_{0.30}Fe_{0.95}Cr_{0.05}O_3$		1.566(7) [0.07]	11.538(1)	98.900(1)
$LaFeO_3$	200 K	1.043(9) [0.05]	17.028(8)	5061.945(8)
$La_{0.70}Eu_{0.30}FeO_3$		1.867(6) [0.08]	11.595(5)	2086.025(5)
$La_{0.70}Eu_{0.30}Fe_{0.95}Cr_{0.05}O_3$		1.708(6) [0.08]	9.470(7)	3239.720(7)
$LaFeO_3$	100 K	1.021(7) [0.04]	13.365(8)	8782.325(8)
$La_{0.70}Eu_{0.30}FeO_3$		2.027(3) [0.09]	9.218(9)	3775.390(9)
$La_{0.70}Eu_{0.30}Fe_{0.95}Cr_{0.05}O_3$		1.856(4) [0.08]	5.343(9)	5008.875(9)
$LaFeO_3$	4 K	1.038(5) [0.05]	5.051(5)	8523.250(5)
$La_{0.70}Eu_{0.30}FeO_3$		2.642(6) [0.12]	1.109(7)	1838.700(7)
$La_{0.70}Eu_{0.30}Fe_{0.95}Cr_{0.05}O_3$		2.457(7) [0.11]	0.700(1)	2221.600(1)

Table 4. The maximum magnetization (M_{max}), coercivity (H_c), and exchange bias (*EB*) of the mechano-synthesized $LaFeO_3$, $La_{0.70}Eu_{0.30}FeO_3$ and $La_{0.70}Eu_{0.30}Fe_{0.95}Cr_{0.05}O_3$ nanoparticles at 300 K, 200 K, 100 K and 4 K. Estimated errors are given in parentheses.
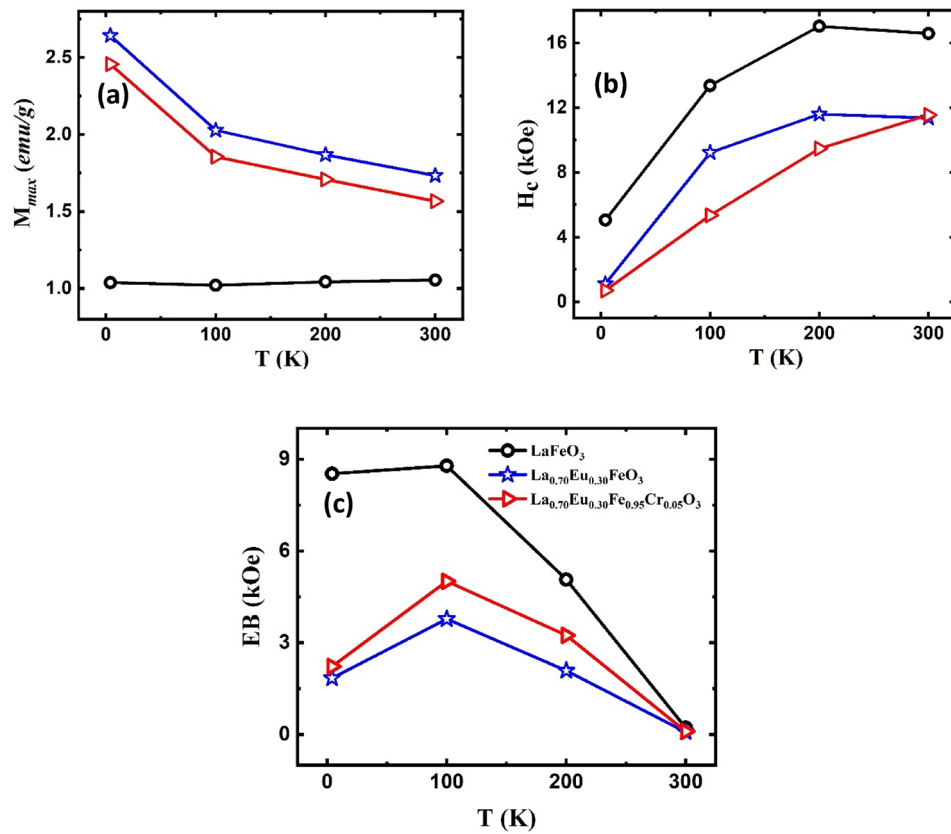

Figure 11. The thermal variation of (**a**) the maximum magnetization (M_{max}), (**b**) coercivity (H_c) and (**c**) exchange bias field (*EB*) for the $LaFeO_3$, $La_{0.70}Eu_{0.30}FeO_3$ and $La_{0.70}Eu_{0.30}Fe_{0.95}Cr_{0.05}O_3$ nanoparticles. The symbols in all figures are as shown in the legend of (**c**).

the temperature dependence of H_c in Fig. 11b that, rather than becoming magnetically harder with decreasing temperature, the mechano-synthesized $LaFeO_3$ and $La_{0.70}Eu_{0.30}FeO_3$ nanoparticles softened as the temperature decreased from 200 to 4 K. For the $La_{0.70}Eu_{0.30}Fe_{0.95}Cr_{0.05}O_3$ nanoparticles, this range extends to 300–4 K. Such an unusual thermal dependence of H_c has been reported before for sol–gel prepared $LaFeO_3$ nanoparticles, where the coercivity was found to decrease by *ca.* 15% upon cooling from 220 to 5 K[49]. In the present case, H_c for the $LaFeO_3$ and $La_{0.70}Eu_{0.30}FeO_3$ has been significantly reduced by *ca.* 70% and 90%, respectively, between 200 and 4 K. For the $La_{0.70}Eu_{0.30}Fe_{0.95}Cr_{0.05}O_3$, it has dropped by ~ 95% as the temperature was changed from 300 to 4 K.

This anomalous magnetic softening may be attributed to the competition between the magnetic anisotropy and magnetoelectric coupling in these multiferroic nanoparticles, which reduces the effective magnetic anisotropy[56].

The negative H_c shifts in the M-H loops for all the samples (Fig. 10) imply the presence of an exchange bias (EB) anisotropy. This is further evidence that the nanoparticles are composed of AFM cores and FM-like shells because EB is known to develop owing to the competition between the exchange and Zeeman energies at the interface of both magnetic structures[49]. The values of the EB fields, EB ($= (H_{c1} + H_{c2})/2$), for the different nanoparticles are listed in Table 4, and their thermal variation is depicted in Fig. 11c. It can be observed that the EB fields increased, reaching a maximum value at 100 K, and then decreased with increasing temperature. The temperature dependence of the EB fields can be related to the thermal activation of the spin reversal in the AFM cores of the particles, which plays a significant role in inducing EB anisotropy in the FM/AFM interfaces of the nanoparticles[13,52]. Initially, the applied field induced a preferred spin alignment in some nanoparticles. When the field direction is reversed, the spins in some nanoparticles, particularly those with large volumes, may not gain sufficient thermal energy to reverse direction. Consequently, the core spins of these nanoparticles did not contribute to the hysteresis loop during the entire cycle, thereby inducing spontaneous EB anisotropy[13]. This may explain why the $LaFeO_3$ nanoparticles, which had the largest particle size and size distribution, as shown in Fig. 2, had the highest EB fields relative to the doped nanoparticles. Throughout the temperature range investigated, the lowest EB values were recorded for $La_{0.70}Eu_{0.30}FeO_3$ nanoparticles. As the EB field values in Fig. 11c reflect the strength of the exchange magnetic coupling, it is evident that doping with Eu^{3+} ions weakens the coupling in the AFM cores. The sharp suppression of EB in the doped nanoparticles at 4 K may demonstrate the robust low-temperature impact of the relatively small amount of surface Eu^{2+} ions, as indicated by the susceptibility analysis above. The slight increase in the EB field values for the $La_{0.70}Eu_{0.30}Fe_{0.95}Cr_{0.05}O_3$ nanoparticles relative to those of $La_{0.70}Eu_{0.30}FeO_3$ may be attributed to the distribution of the dopant Cr^{3+} ions in the $La_{0.70}Eu_{0.30}FeO_3$ ionic matrix, where the formation of the $Cr^{3+}–O^{2-}–Cr^{3+}$ AFM superexchange interaction is more favorable[13] than that of $Fe^{3+}–O^{2-}–Cr^{3+}$. This in turn strengthens the overall exchange coupling within the AFM cores. As a final comment in this section, we note that the present mechano-synthesized $LaFeO_3$ nanoparticles show higher EB fields than those of similar sizes prepared using other synthesis routes. For example, at 300 K, the EB value was ~ 217 Oe relative to 139 Oe for $LaFeO_3$ nanoparticles prepared via the sol–gel route[57] and ~ 8.523 kOe (4 K) relative to 1.205 kOe (5 K)[49]. Apparently, this is related to the complex surface composition induced by the mechano-synthesis route, as discussed in section "Surface composition: XPS spectral analysis", which has no counterpart in the case of $LaFeO_3$ nanoparticles prepared using other techniques.

Conclusion

Single-phase perovskite-related $LaFeO_3$, $La_{0.70}Eu_{0.30}FeO_3$ and $La_{0.70}Eu_{0.3}Fe_{0.95}Cr_{0.05}O_3$ nanoparticles (20–50 nm) were mechano-synthesized at 600 °C (10 h) for the pure and 700 °C (10 h) for the two variants. These temperatures are substantially lower by ~ 600–700 °C than those at which the corresponding bulk materials are traditionally synthesized using solid-state methods. Upon Eu^{3+} doping and Eu^{3+}/Cr^{3+} co-doping, the perovskite-related orthorhombic $LaFeO_3$ structure undergoes a transition from the usual O′-type distorted orthorhombic structure of orthoferrites to the O-type structure. Eu^{3+} ions preferentially occupy the A-sites in the crystal structure of $LaFeO_3$, whereas Cr^{3+} ions are randomly distributed over the octahedral B-sites, and the bond angles and lengths are sensitive to doping and co-doping. Both ^{57}Fe Mössbauer and magnetic measurements suggested that the nanoparticles were composed of dominant canted AFM cores and FM shells because of uncompensated surface spins, and no superparamagnetism was observed. The increase in ZFC magnetization of the $LaFeO_3$ nanoparticles at relatively low temperatures is attributed to the resistance of the core spins; hence, the local spin order that develops at the interface between the canted AFM cores and FM shells is to be aligned by the applied magnetic field. The magnetization of the nanoparticles was sensitive to the presence of Eu^{3+} and Cr^{3+} ions. The $La_{0.70}Eu_{0.30}FeO_3$ and $La_{0.70}Eu_{0.30}Fe_{0.95}Cr_{0.05}O_3$ nanoparticles were found to display Eu^{3+} van-Vleck-type paramagnetic molar susceptibility with a spin–orbit coupling constant of 363 cm^{-1} in the ~ 20–300 K range and a Curie–Weiss like behavior below 20 K due to the minority of the surface Eu^{2+} ions. The θ_W and μ_{eff} values obtained at low temperatures for the Eu-doped nanoparticles suggest a weak AFM interaction between the Eu^{2+} ions and the Eu^{2+}/Eu^{3+} valence state fluctuations, hence the absence of localized Eu magnetic moments. All nanoparticles exhibited anomalous magnetic softening with decreasing temperature, which is referred to as the competition between magnetic anisotropy and magnetoelectric coupling. The nanoparticles reveal temperature-dependent dopant-sensitive exchange bias fields that manifest their AFM/FM core–shell nature, reflecting the thermal activation of the spin reversal at their cores.

Data availability

The datasets used and/or analyzed during the current study available from the corresponding author on reasonable request.

References

1. Fujii, T., Matsusue, I. & Takada, J. Superparamagnetic behaviour and induced ferrimagnetism of $LaFeO_3$ nanoparticles prepared by a hot-soap technique. *Adv. Aspects Spectrosc.* **373**, 373–390 (2012).
2. Köferstein, R., Jäger, L. & Ebbinghaus, S. G. Magnetic and optical investigations on $LaFeO_3$ powders with different particle sizes and corresponding ceramics. *Solid State Ion.* **249–250**, 1–5 (2013).
3. Mukhopadhyay, K., Mahapatra, A. S. & Chakrabarti, P. K. Multiferroic behavior, enhanced magnetization and exchange bias effect of Zn substituted nanocrystalline LaFeO3 ($La_{(1-x)}Zn_xFeO_3$, x = 0.10, and 0.30). *J. Magn. Magn. Mater.* **329**, 133–141 (2013).

4. Sasikala, C. *et al.* Transition metal titanium (Ti) doped LaFeO$_3$ nanoparticles for enhanced optical structural and magnetic properties. *J. Alloys Compd.* **712**, 870–877 (2017).
5. Treves, D. Studies on orthoferrites at the Weizmann Institute of Science. *J. Appl. Phys.* **36**, 1033–1039 (1965).
6. Al-Mamari, R. T. *et al.* Structural, Mössbauer, and optical studies of mechano-synthesized Ru^{3+}-doped LaFeO$_3$ nanoparticles. *Hyperfine Interact.* **243**, 1–12 (2021).
7. Triyono, D., Hanifah, U. & Laysandra, H. Structural and optical properties of Mg-substituted LaFeO$_3$ nanoparticles prepared by a sol-gel method. *Results Phys.* **16**, 1–8 (2020).
8. Marezio, M., Remeika, J. P. & Dernier, P. D. IUCr, the crystal chemistry of the rare earth orthoferrites. *Acta Crystallogr. Sect. B* **26**, 2008–2022 (1970).
9. Lakshmana Rao, T. *et al.* Substitution induced magnetic phase transitions and related electrical conduction mechanisms in LaFeO$_3$ nanoparticle. *J. Appl. Phys.* **126**, 1–8 (2019).
10. Lakshmana Rao, T., Pradhan, M. K., Singh, S. & Dash, S. Influence of Zn(II) on the structure, magnetic and dielectric dynamics of nano-LaFeO$_3$. *J. Mater. Sci. Mater. Electron.* **31**, 4542–4553 (2020).
11. Shikha, P., Kang, T. S. & Randhawa, B. S. Effect of different synthetic routes on the structural, morphological and magnetic properties of Ce doped LaFeO$_3$ nanoparticles. *J. Alloys Compd.* **625**, 336–345 (2015).
12. Hosseini, S. A. *et al.* Synthesis, characterization, and catalytic activity of nanocrystalline La$_{1-x}$Eu$_x$FeO$_3$ during the combustion of toluene. *Chin. J. Catal.* **32**, 1465–1468 (2011).
13. Blessington Selvadurai, A. P. *et al.* Influence of Cr substitution on structural, magnetic and electrical conductivity spectra of LaFeO$_3$. *J. Alloys Compd.* **646**, 924–931 (2015).
14. Bhame, S. D., Joly, V. L. J. & Joy, P. A. Effect of disorder on the magnetic properties of LaMn$_{0.5}$Fe$_{0.5}$O$_3$. *Phys. Rev.* **72**, 1–7 (2005).
15. Al-Rashdi, K. S. *et al.* Structural, ^{57}Fe Mössbauer and XPS studies of mechano-synthesized nanocrystalline Nd$_{0.33}$Eu$_{0.67}$Fe$_{1-x}$Cr$_x$O$_3$ particles. *Mater. Res. Bull.* **132**, 1–12 (2020).
16. Da Silva, K. L. *et al.* Mechano-synthesized BiFeO$_3$ nanoparticles with highly reactive surface and enhanced magnetization. *J. Phys. Chem. C* **115**, 7209–7217 (2011).
17. Mahmood, A., Warsi, M. F., Ashiq, M. N. & Ishaq, M. Substitution of La and Fe with Dy and Mn in multiferroic La$_{1-x}$Dy$_x$Fe$_{1-y}$Mn$_y$O$_3$ nanocrystallites. *J. Magn. Magn. Mater.* **327**, 64–70 (2013).
18. Mitra, A. *et al.* Simultaneous enhancement of magnetic and ferroelectric properties of LaFeO$_3$ by co-doping with Dy^{3+} and Ti^{4+}. *J. Alloys Compd.* **726**, 1195–1204 (2017).
19. Natali Sora, I. *et al.* Crystal structures and magnetic properties of strontium and copper doped lanthanum ferrites. *J. Solid State Chem.* **191**, 33–39 (2012).
20. Larson, A. C. & Dreele, R. B. General structure analysis system "GSAS". Los Alamos National Laboratory Report No., LAUR 86–748 (2000).
21. Fairley, N. *et al.* Systematic and collaborative approach to problem solving using X-ray photoelectron spectroscopy. *Appl. Surf. Sci. Adv.* **5**, 1–9 (2021).
22. Acharya, S., Mondal, J., Ghosh, S., Roy, S. K. & Chakrabarti, P. K. Multiferroic behavior of lanthanum orthoferrite (LaFeO$_3$). *Mater. Lett.* **64**, 415–418 (2010).
23. Popa, N. C. & Balzar, D. An analytical approximation for a size-broadened profile given by the lognormal and gamma distributions. *J. Appl. Crystallogr.* **35**, 338–346 (2002).
24. Momma, K. & Izumi, F. VESTA 3 for three-dimensional visualization of crystal, volumetric and morphology data. *J. Appl. Crystallogr.* **44**, 1272–1276 (2011).
25. Widatallah, H. M. *et al.* Formation, cationic site exchange and surface structure of mechano-synthesized EuCrO$_3$ nanocrystalline particles. *J. Phys. D Appl. Phys.* **44**, 1–9 (2011).
26. WebElements. https://www.webelements.com
27. Knížek, K. *et al.* Structural anomalies associated with the electronic and spin transitions in LnCoO$_3$. *Eur. Phys. J. B* **47**, 213–220 (2005).
28. Pekinchak, O., Vasylechko, L., Berezovets, V. & Prots, Y. Structural Behaviour of EuCoO$_3$ and mixed cobaltites-ferrites EuCo$_{1-x}$Fe$_x$O$_3$. *Solid State Phenom.* **230**, 31–38 (2015).
29. Glazer, A. M. IUCr, the classification of tilted octahedra in perovskites. *Acta Crystallogr. Sect. B: Struct. Crystallogr. Cryst. Chem.* **28**, 3384–3392 (1972).
30. Smirnova, I. S. *et al.* IR-active optical phonons in Pnma-1, Pnma-2 and R3c phases of LaMnO$_{3+\delta}$. *Phys. B* **403**, 3896–3902 (2008).
31. Stuart, B. H. *Infrared Spectroscopy: Fundamentals and Applications* (Wiley, 2004).
32. Rao, G. V. S., Rao, C. N. R. & Ferraro, J. R. Infrared and electronic spectra of rare earth perovskites: Ortho-chromites, -manganites and -ferrites. *Appl. Spectrosc.* **24**, 436–445 (1970).
33. Pence, H. E. & Williams, A. ChemSpider: An online chemical information resource. *J. Chem. Educ.* **87**, 1123–1124 (2010).
34. Greenwood, N. N. & Gibb, T. C. *Mössbauer Spectroscopy* (Chapman and Hall Ltd, 1971).
35. Kuznetsov, M. V., Pankhurst, Q. A., Parkin, I. P. & Morozov, Y. G. Self-propagating high-temperature synthesisof chromium substituted lanthanum orthoferrites LaFe$_{1-x}$Cr$_x$O$_3$ ($0 \le x \le 1$). *J. Mater. Chem.* **11**, 854–858 (2001).
36. Cao, E. *et al.* Enhanced ethanol sensing performance of Au and Cl comodified LaFeO$_3$ nanoparticles. *ACS Appl. Nano Mater.* **2**, 1541–1551 (2019).
37. Moulder, J. F., Stickle, W. F., Sobol, P. E. & Bomben, K. D. In *Handbook of X-ray Photoelectron Spectroscopy* (ed. Chastain, J.) (Perkin-Elmer Corporation, Physical Electronics Division, 1992).
38. Lee, Y. *et al.* Hydrogen barrier performance of sputtered La$_2$O$_3$ films for InGaZnO thin-film transistor. *J. Mater. Sci.* **54**, 11145–11156 (2019).
39. Qin, L. *et al.* Improved cyclic redox reactivity of lanthanum modified iron-based oxygen carriers in carbon monoxide chemical looping combustion. *J. Mater. Chem. A* **5**, 20153–20160 (2017).
40. Schaffer, J. P., Saxena, A., Antolovich, S. D., Sanders, T. H. J. & Warner, S. B. *The Science and Design of Engineering Materials* 2nd edn. (WCB/McGraw-Hill, WCB, 1999).
41. Mills, P. & Sullivan, J. L. A study of the core level electrons in iron and its three oxides by means of X-ray photoelectron spectroscopy. *J. Phys. D Appl. Phys.* **16**, 723–732 (1983).
42. Huang, S. *et al.* High-temperature colossal dielectric response in RFeO$_3$ (R = La, Pr and Sm) ceramics. *Ceram. Int.* **41**, 691–698 (2015).
43. Ye, J. L., Wang, C. C., Ni, W. & Sun, X. H. Dielectric properties of ErFeO$_3$ ceramics over a broad temperature range. *J. Alloys Compd.* **617**, 850–854 (2014).
44. Polat, O. *et al.* Electrical characterization of Ir doped rare-earth orthoferrite YbFeO$_3$. *J. Alloys Compd.* **787**, 1212–1224 (2019).
45. Cao, E. *et al.* Enhanced ethanol sensing performance for chlorine doped nanocrystalline LaFeO$_{3-\delta}$ powders by citric sol-gel method. *Sens. Actuators B Chem.* **251**, 885–893 (2017).
46. Freyria, F. S. *et al.* Eu-doped α-Fe$_2$O$_3$ nanoparticles with modified magnetic properties. *J. Solid State Chem.* **201**, 302–311 (2013).
47. Cho, E.-J. & Oh, S.-J. Surface valence transition in trivalent Eu insulating compounds observed by photoelectron spectroscopy. *Phys. Rev. B* **59**, 15613–15616 (1999).
48. Ranaut, D. & Mukherjee, K. Van Vleck paramagnetism and enhancement of effective moment with magnetic field in rare earth orthovanadate EuVO$_4$. *Phys. Lett. A* **465**, 128710 (2023).

16

49. Ahmadvand, H. *et al.* Exchange bias in LaFeO$_3$ nanoparticles. *J. Phys. D Appl. Phys.* **43**, 1–5 (2010).
50. El-Moez, A., Mohamed, A., Álvarez-Alonso, P. & Hernando, B. The intrinsic exchange bias effect in the LaMnO$_3$ and LaFeO$_3$ compounds. *J. Alloys Compd.* **850**, 1–8 (2021).
51. Widatallah, H. M. *et al.* Structural, magnetic and ^{151}Eu Mössbauer studies of mechano-synthesized nanocrystalline EuCr$_{1-x}$Fe$_x$O$_3$ particles. *Acta Mater.* **61**, 4461–4473 (2013).
52. Paul, P., Ghosh, P. S., Rajarajan, A. K., Babu, P. D. & Rao, T. V. C. Ground state spin structure of GdFeO$_3$: A computational and experimental study. *J. Magn. Magn. Mater.* **518**, 167407 (2020).
53. Warshi, M. K. *et al.* Cluster glass behavior in orthorhombic SmFeO$_3$ perovskite: Interplay between spin ordering and lattice dynamics. *Chem. Mater.* **32**, 1250–1260 (2020).
54. Dash, B. B. & Ravi, S. Structural, magnetic and electrical properties of Fe substituted GdCrO$_3$. *Solid State Sci.* **83**, 192–200 (2018).
55. Nogués, J. & Schuller, I. K. Exchange bias. *J. Magn. Magn. Mater.* **192**, 203–232 (1999).
56. Ahmmad, B., Islam, M. Z., Billah, A. & Basith, M. A. Anomalous coercivity enhancement with temperature and tunable exchange bias in Gd and Ti co-doped BiFeO$_3$ multiferroics. *J. Phys. D Appl. Phys.* **49**, 09 (2016).
57. Stoner, E. C. & Wohlfarth, E. P. A mechanism of magnetic hysteresis in heterogeneous alloys. *Philos. Trans. R. Soc. Lond. Ser. A* **240**, 599–642 (1948).

Acknowledgements

Author contributions

R.T.A. did the experimental investigation, analysis, conceptualization and wrote the initial draft. H.M.W. proposed and supervised the project, contributed to the analysis and the conceptualization, wrote the final draft. M.E.E. co-supervised the project and reviewed the manuscript. A.M.G contributed to the Mossbauer measurements and analysis. A.D.A co-supervised the project and reviewed the manuscript. S.H.A. provided laboratory resources and contributed to the XPS analysis and reviewed the manuscript. M.T.Z.M did XPS measurements. N.A. reviewed the final manuscript and MA provided laboratory resources and reviewed the manuscript.

Competing interests

The authors declare no competing interests.

Additional information

Supplementary Information The online version contains supplementary material available at https://doi.org/10.1038/s41598-024-65757-z.

Correspondence and requests for materials should be addressed to H.M.W.

Reprints and permissions information is available at www.nature.com/reprints.

Publisher's note Springer Nature remains neutral with regard to jurisdictional claims in published maps and institutional affiliations.